RSC Advances

PAPER

View Article Online
View Journal | View Issue

Cite this: *RSC Adv.*, 2024, **14**, 31193

Ball-milling preparation of $ZnFe_2O_4$/AgI nanocomposite with enhanced photocatalytic activity†

Meiling Liu,[a] Yan Quan,[a] Mengjie Feng,[a] Chunguang Ren*[b] and Zhonghua Wang *[a]

Received 31st July 2024
Accepted 24th September 2024

DOI: 10.1039/d4ra05539j

rsc.li/rsc-advances

Semiconductor photocatalytic technology is increasingly being utilized in wastewater treatment due to its high efficiency, low energy consumption and environmental friendliness. However, single photocatalysts often exhibit low catalytic performance. In this study, a $ZnFe_2O_4$/AgI composite photocatalyst was initially prepared using a high-energy ball-milling method. For the first time, it was applied to the photocatalytic dehydrogenation of diethyl 1,4-dihydro-2,6-dimethylpyridine-3,5-dicarboxylate (1,4-DHP), as well as photocatalytic degradation of harmful substances such as amaranth (AM), methyl orange (MO) and indole present in wastewater. The composite photocatalyst exhibited superior catalytic performance compared to $ZnFe_2O_4$ and AgI under visible light irradiation ($\lambda \geq 400$ nm). With optimized composition, the pseudo-first-order rate constants of $ZnFe_2O_4$/AgI-50% were approximately 6, 20, 64 and 38 times higher than that of AgI for the photooxidation of 1,4-DHP, AM, MO and indole, respectively. The enhanced catalytic activity of the composite was attributed to the formation of heterojunction between $ZnFe_2O_4$ and AgI, which facilitated the separation and transfer of photogenerated charge carriers. Mechanism studies revealed that photogenerated holes (h^+) and superoxide radical anions ($^{\bullet}O_2^-$) played pivotal roles in the photocatalytic reaction process.

Introduction

Semiconductor-based photocatalysis has been extensively studied for their critical role in environmental remediation and renewable clean energy technologies since its initial discovery.[1–3] For example, it can be used for dyes degradation such as MB and MO,[4,5] reduction of Cr(VI),[6,7] reduction of CO_2,[8,9] and other fields.[10] However, a single photocatalyst inevitably encounters certain challenges, such as weak redox abilities of photoinduced electrons (e^-) and holes (h^+),[11] poor capacity for visible light adsorption and fast recombination of charge carriers.[12] To address these unfavorable factors and further enhance the photocatalytic performance of a single semiconductor, an effective strategy is to introduce another photocatalyst to construct a heterojunction composite.[13,14]

Spinel zinc ferrite ($ZnFe_2O_4$) has attracted significant attention in the field of photocatalysis due to its strong magnetic recyclability,[15,16] high photochemical stability,[17] narrow band gap (~1.9 eV),[13,18] visible-light activity,[19] and environmental friendliness.[20,21] Despite extensive investigations into the photocatalytic performances of $ZnFe_2O_4$ with different morphologies and sizes,[22,23] it has been found that a single component of $ZnFe_2O_4$ often exhibits unsatisfactory photocatalytic activity, sometimes even showing nearly no catalytic effect.[13,24] This is attributed to the rapid recombination of photogenerated e^-–h^+ pairs[25,26] under light irradiation, which marvelously hinders its practical applications. Nevertheless, it has been demonstrated that the construction of $ZnFe_2O_4$ with other semiconductors through the formation of heterojunction structure can effectively improve its activity.[13,15,27] For example, Zhang *et al.* prepared $ZnFe_2O_4$/BiOI hybrid photocatalysts using the solvothermal method. While single $ZnFe_2O_4$ exhibited negligible photocatalytic activity, the 5%-$ZnFe_2O_4$/BiOI composite showed optimal degradation efficiency (81.2%) within 100 minutes under visible light irradiation.[20] Similarly, Dai *et al.* synthesized magnetic $ZnFe_2O_4$@ZnSe hollow nanospheres using a two-step method and utilized them for the photocatalytic splitting of water. Despite the negligible photocatalytic activity of pure $ZnFe_2O_4$, the $ZnFe_2O_4$@ZnSe-20 composite exhibited high hydrogen production under light irradiation.[28]

Silver-containing materials have been extensively studied and utilized in various fields, including biomedical application,[29] antibacterial agents,[30,31] photocatalysis,[30,32] water disinfection,[33] and other related fields.[34,35] Silver iodide (AgI) has garnered significant attention as a photocatalyst due to its exceptional electrical conductivity, strong absorption of visible

[a]*Chemical Synthesis and Pollution Control Key Laboratory, College of Chemistry and Chemical Engineering, China West Normal University, Nanchong 637002, Sichuan, China. E-mail: zhwangs@163.com*

[b]*School of Pharmacy, Yantai University, Yantai 264005, Shandong, China. E-mail: cgren@ytu.edu.cn; Fax: (+86) 817-2445233; Tel: (+86) 817-2568081*

† Electronic supplementary information (ESI) available. See DOI: https://doi.org/10.1039/d4ra05539j

light,[36] and a narrow band gap (~2.8 eV).[37,38] However, pure AgI is unstable under light irradiation and can easily be reduced to metallic silver (Ag), which weakens its catalytic activity.[39] To improve the stability of AgI, it can be composited with other materials.[36,37,39] For example, Xu and coworkers have firstly prepared $ZnFe_2O_4$/AgI composites successfully with a hydrothermal method, and found that $ZnFe_2O_4$ nanoparticles were uniformly decorated on the surface of AgI particles. The obtained composite catalysts exhibited excellent photocatalytic disinfection of *E. coli* and degradation of rhodamine B under visible light irradiation due to enhanced the light harvesting ability and improved the separation efficiency of the photogenerated charge carriers.[37]

Ball milling method is a mechanical technique utilized for the purpose of grinding powders into fine particles.[40] Additionally, it can cause changes in the structure, oxygen vacancy and even trigger chemical reactions.[32,41] In recent time, ball milling method has been widely employed for the large-scale preparation of various catalytic materials due to its simplicity, scalability, low cost and environmental friendliness.[42,43] In this study, $ZnFe_2O_4$/AgI composites with varying mass proportions of AgI and $ZnFe_2O_4$ were prepared using the ball-milling method. The photocatalytic performance of the ball-milling prepared $ZnFe_2O_4$/AgI composite was assessed by the dehydrogenation 1,4-DHP and photocatalytic degradation of AM, MO and indole. Furthermore, we compared the photocatalytic performance of the ball-milling prepared $ZnFe_2O_4$/AgI composite with that of counterparts prepared *via* deposition–precipitation and a simple mixture of $ZnFe_2O_4$/AgI. The primary reactive species involved in the photocatalytic process were examined through the application of various chemical scavengers and the electron spin resonance (ESR) technique.

Experimental methods

Materials

The materials information is provided in the ESI (Section 1).†

Synthesis of $ZnFe_2O_4$/AgI composites

Detailed preparation of $ZnFe_2O_4$ and AgI can be found in the ESI (Section 2).†

$ZnFe_2O_4$/AgI composites were prepared by a ball milling method. Typically, the mass ratio of ball to material is 25 : 1. Specifically, 0.2 g $ZnFe_2O_4$ and 0.2 g AgI were mixed and placed in a stainless-steel jar, which was fixed on a planetary ball mill (XGB04 type). The $ZnFe_2O_4$ and AgI mixture was continuously milled with stainless steel balls in the jar for 2 h at 400 rpm. This sample was labeled as $ZnFe_2O_4$/AgI-50% (ZA-50%), for the mass percentage of AgI was 50%. Other $ZnFe_2O_4$/AgI composites were prepared using the same procedure as described above, with varying mass proportion of AgI while maintaining the total mass at 0.4 g. The resulted composites were denoted as $ZnFe_2O_4$/AgI-*x*% or ZA-*x*% (where *x* represents the mass percentage of AgI).

In order to further confirm the high efficiency of the ball milling method, the best proportion ZA-50% was used as comparation. ZA-50% composite prepared by deposition–precipitation method (DP-ZA-50%) was carried out as following: 80 mg of previously synthesized $ZnFe_2O_4$ was weighed and added to 30 mL of DI for ultrasonic dispersion. Then, 3.4 mL of $AgNO_3$ (0.1 mol L^{-1}) and 1.7 mL of KI (0.2 mol L^{-1}) were added dropwise, followed by stirred for 1 h. The precipitate was collected by centrifugation, washed three times using deionized (DI) water and dried at 60 °C. For simple mixing, 25 mg each of $ZnFe_2O_4$ and AgI were weighed and thoroughly mixed using a glass rod. The resulting sample was designated as SM-ZA-50%.

Characterization

The characterization information is provided in the ESI (Section 3).†

Photocatalytic evaluation

The photocatalytic performance of $ZnFe_2O_4$/AgI composites was evaluated by the photooxidative dehydrogenation of 1,4-DHP (0.1 mmol L^{-1}) in a solution prepared with EtOH and DI water (v/v = 1 : 1).[44,45] The dehydrogenation efficiency was determined by measuring the absorbance at 374 nm.[46] In a beaker, 50 mg of $ZnFe_2O_4$/AgI sample and 50 mL of 1,4-DHP solution were mixed and stirred for 30 minutes under dark condition to achieve an absorption–desorption equilibrium. After equilibrium, about 2.5 mL of the reaction suspension was taken and filtered through a 0.22 μm filter to remove the photocatalyst. The beaker was then placed under a metal halide lamp (70 W) with a UV cut-off filter ($\lambda \geq 400$ nm) to obtain visible light. Samples were taken every minute and tested the absorbance using a Shimadzu UV-2550 spectrophotometer.

The degradation process of amaranth (AM, 30 mg L^{-1}), methyl orange (MO, 10 mg L^{-1}), and indole (20 mg L^{-1}) followed a similar procedure to that of 1,4-DHP. However, the absorbance measurements were taken at different wavelengths: 520 nm[47] for AM, 464 nm[5] for MO, and 270 nm[48] for indole.

Photoelectrochemical measurements

The photoelectrochemical measurements were performed on a CHI 760E electrochemical workstation with a typical three-

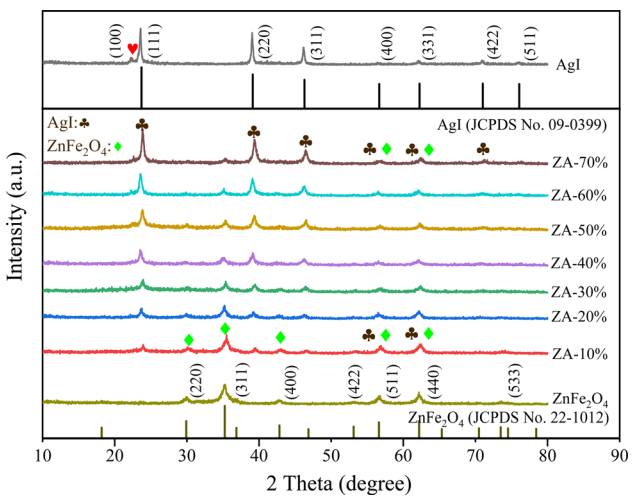

Fig. 1 XRD patterns of AgI, $ZnFe_2O_4$ and $ZnFe_2O_4$/AgI composites.

electrode cell. Visible light was generated by a 300 W xenon lamp equipped with a 400 nm cut-off filter. The working electrode was prepared by drop-casting the photocatalyst onto ITO conductive glass. A platinum (Pt) wire and a silver/silver chloride (Ag/AgCl) electrode were used as the counter electrode and reference electrode, respectively. A Na_2SO_4 solution (0.2 mol L^{-1}) was utilized as the electrolyte.

The photocurrent time (*i*–*t*) curves were obtained under a typical switching cycle of intermittent visible light illumination with a bias voltage of 0.8 V. The photocurrent was recorded by turning the visible light on or off for a duration of 20 s. Additionally, the electrical impedance spectroscopy diagram (EIS) was performed with an amplitude of 5 mV at a potential of 1.38 V in the frequency range of 0.1 to 100 kHz. Mott–Schottky plots were carried at 1 kHz, and the measured potentials *versus* Ag/AgCl were converted to the normal hydrogen electrode (NHE) scale by the equation of $E_{NHE} = E_{Ag/AgCl} + 0.197$ V.

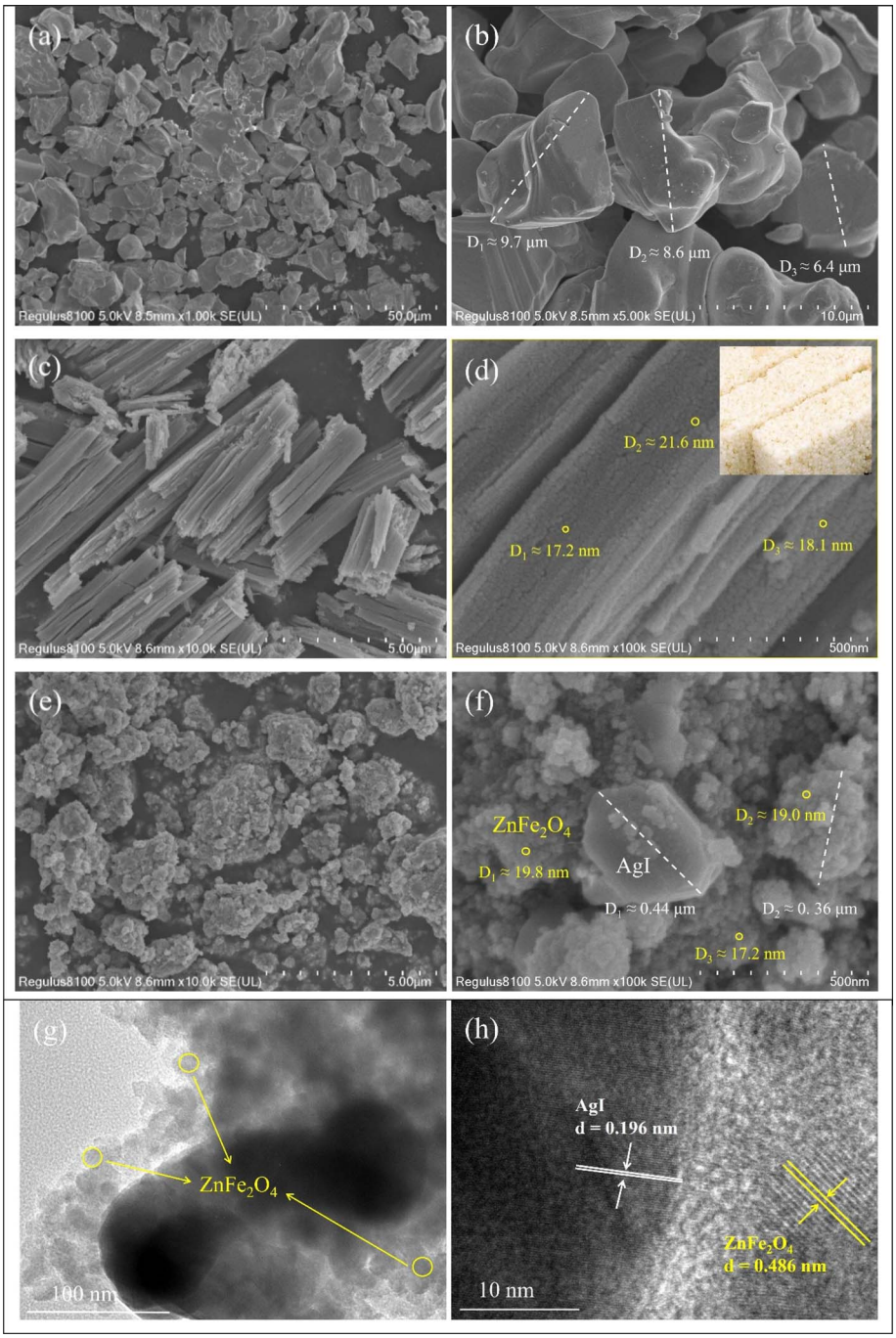

Fig. 2 SEM images with different magnifications: AgI (a and b), $ZnFe_2O_4$ (c and d) and ZA-50% (e and f); TEM (g) and HRTEM (h) images with lattice fringes of AgI and $ZnFe_2O_4$ highlighted in the figure.

Photocatalytic mechanism

In order to elucidate the principle of dehydrogenation of 1,4-DHP and decolorization of AM by this composite, active species capture experiments were performed. EDTA-2Na (10 mmol L^{-1}) and IPA (10 mmol L^{-1}) were used as a hole (h^+) trapping agent and hydroxyl radical ($^{\cdot}OH$) trapping agent, respectively. N_2 was introduced to remove dissolved oxygen and to investigate the role of $^{\cdot}O_2^-$.

Results and discussion

Structure and morphology characterization of photocatalysts

Fig. 1 shows the XRD patterns of $ZnFe_2O_4$, AgI and $ZnFe_2O_4$/AgI composites. The diffraction peaks of $ZnFe_2O_4$ correspond to the cubic crystal phase, with distinct diffraction peaks at 2θ values of 29.92° (220), 35.26° (311), 42.84° (400), 53.11° (422), 56.63° (511), 62.21° (440), and 73.51° (533). These values are in good agreement with the standard data of $ZnFe_2O_4$ (JCPDS No. 22-1012).[20] Similarly, AgI exhibits a cubic crystal phase with characteristic peaks at 23.71° (111), 39.13° (220), 46.31° (311), 56.67° (400), 62.26° (331), 71.03° (422), and 76.08° (511) corresponding to AgI (JCPDS No. 09-0399).[28] However, the synthesized AgI shows an additional peak (marked by ♥) when compared to the cubic crystal phase (Fig. 1), which corresponds to a characteristic feature of the hexagonal crystal phase of AgI (JCPDS No. 09-0374):[21,28] 22.32° (100). For the $ZnFe_2O_4$/AgI composites, as the proportion of AgI increased, the characteristic peaks of AgI (marked by ♣) gradually appeared and strengthened while those for $ZnFe_2O_4$ (marked by ◆) showed an opposite trend. Apart from these characteristic diffraction peaks, no impurity peaks were observed. It is worth noting that the diffraction peaks corresponding to specific proportions, such as ZA-70%, exhibited a slight shift towards higher angle regions for the crystal planes of (111), (220), and (311), indicating a reduction in interatomic distance resulting from compressive stress.[49] This phenomenon indicated that $ZnFe_2O_4$ and AgI could cause slight lattice shrinkage during ball milling mixing,[50] but the crystal phase remained unchanged, and pure composite materials were successfully prepared.

To visually observe the microstructure of the samples, SEM test was conducted. As shown in Fig. 2a and b, AgI exhibited a stone-like morphology with a diameter of approximately 5–10 μm. $ZnFe_2O_4$ displayed a distinct rod-shaped structure (Fig. 2c and d), consisting of many small holes with diameters of about 20 nm, arranged in a configuration that resembles rice candy (Fig. 2d, inset). The microstructure of the ZA-50% composite obtained by ball milling method was depicted in Fig. 2e and f, revealing a large number of small particles with diameters of about 20 nm and an obvious stone-like structure. Based on the previously described morphology of AgI and $ZnFe_2O_4$, it was further hypothesized that the small particles were the components of $ZnFe_2O_4$, and the rod-like structure was destroyed after ball milling, leaving only the small particles, and no significant difference in particle size was found.[51] After ball milling, some small particles attached to the stone-like structure of AgI, it can also prove that $ZnFe_2O_4$ and AgI are fully mixed to form composites, and the size of AgI was decreased from 5–10 μm to about 0.4 μm.

In order to further observe the microscopic morphology of the ZA-50% composite, it was further characterized by TEM and

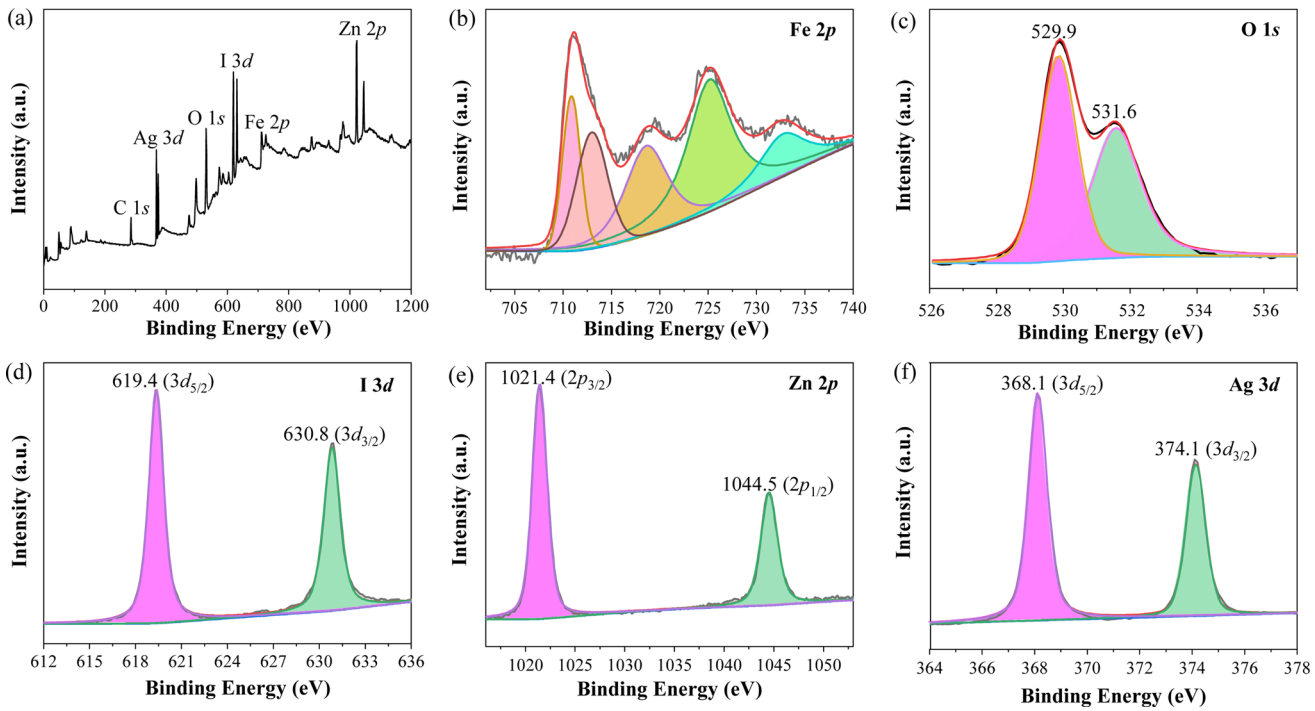

Fig. 3 High-resolution XPS spectra of ZA-50% composite: the complete XPS survey spectrum (a), Fe 2p (b), O 1s (c), I 3d (d), Zn 2p (e) and Ag 3d (f).

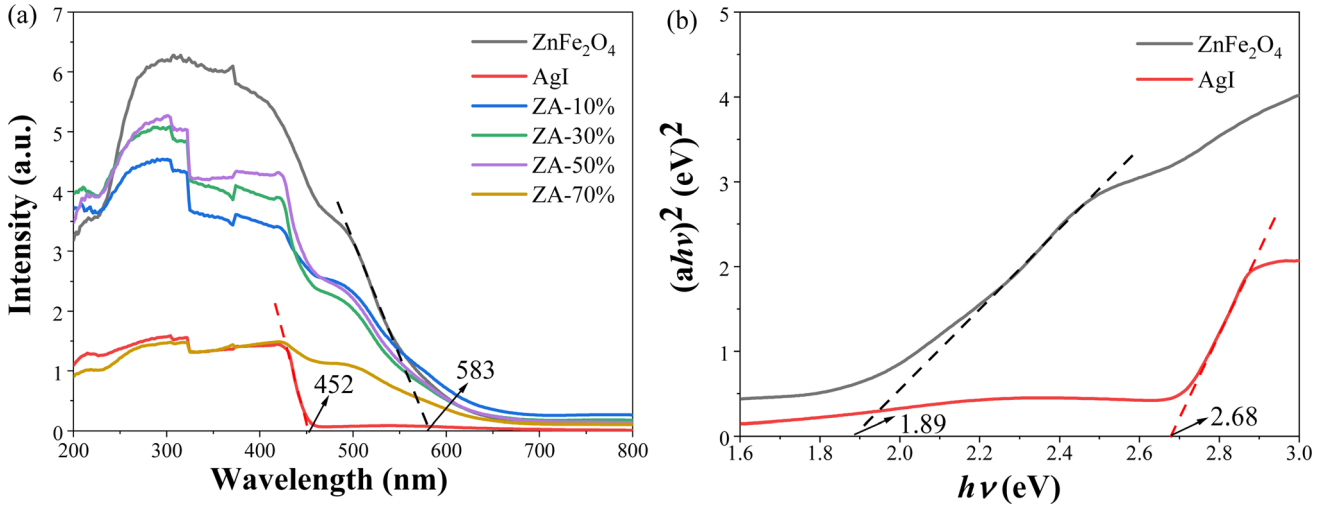

Fig. 4 UV-Vis diffuse reflectance spectra of $ZnFe_2O_4$, AgI and ZA-*x*% (a), calculated band gap of $ZnFe_2O_4$ and AgI with $(\alpha h\nu)^2$ graph of relationship with energy ($h\nu$) (b).

HRTEM. The images in Fig. 2g and h show obvious bright and dark interlacing phenomena indicating that AgI was tightly bound to $ZnFe_2O_4$. In Fig. 2g, the bright area consists of many small particles which were identified as components of $ZnFe_2O_4$ through SEM analysis. Additionally, in Fig. 2h, the (111) crystal surface belonging to $ZnFe_2O_4$ (JCPDS No. 22-1012) was observed in the bright area with a lattice spacing of 0.486 nm.[52,53] On the other hand, the dark area was confirmed as AgI, the (311) crystal surface of AgI was also observed (JCPDS No. 09-0399), where the lattice spacing was measured as 0.196 nm (Fig. 2h). These results collectively indicated that AgI and $ZnFe_2O_4$ were tightly combined to form a heterojunction composite after high-energy mechanical ball milling.

XPS survey spectrum was performed to analyze the chemical compositions of the ZA-50% nanocomposite. As shown in Fig. 3a, It was revealed that the composite comprises Zn, Fe, O,

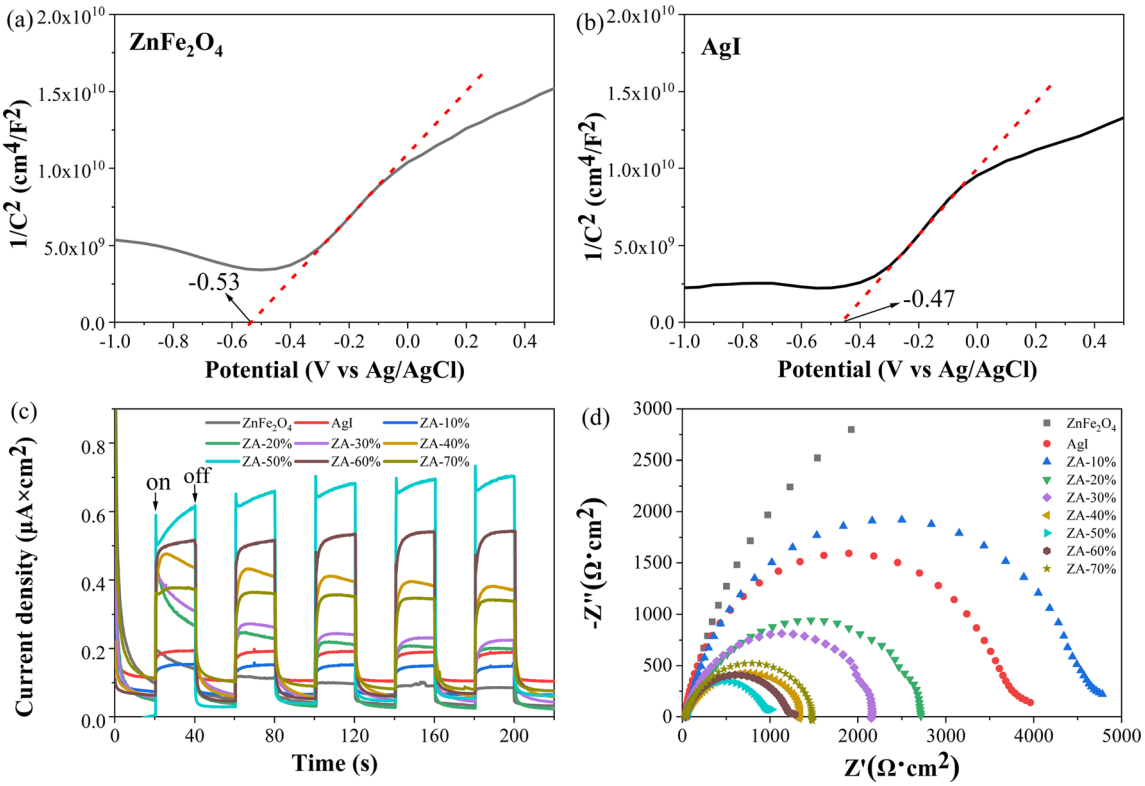

Fig. 5 Mott–Schottky curves of $ZnFe_2O_4$ (a) and AgI (b), transient photocurrent responses (c), EIS Nyquist plots of the $ZnFe_2O_4$, AgI and ZA-*x*% (d).

Ag and I elements. The presence of C 1s (284.8 eV) is attributed to the adventitious hydrocarbon from the XPS instrument itself.[52] The Fe 2p spectrum (Fig. 3b) displayed binding energies at 710.8 and 713.1 eV, which corresponded well with the Fe $2p_{3/2}$.[54,55] Additionally, a peak at binding energy of 725.3 eV aligned closely with the Fe $2p_{1/2}$,[54] while the other peaks at 718.8 and 733.2 eV originated from the shake-up satellite of Fe^{3+}.[56,57] From Fig. 3c, two deconvoluted peaks at 529.9 and 531.6 eV were the indicative of lattice oxygen and the defect sites associated with the absorbed water on the sample surface.[56,58] From Fig. 3d, the high resolution I 3d spectrum of ZA-50% composite exhibited two distinct peaks at 619.4 and 630.8 eV for I $3d_{5/2}$ and I $3d_{3/2}$, respectively.[59] In the Zn 2p spectra (Fig. 3e), peaks at 1021.4 and 1044.5 eV were assigned to Zn $2p_{3/2}$ and Zn $2p_{1/2}$ respectively, which is characteristic of Zn^{2+}.[56,60] The Ag 3d spectrum of ZA-50% displayed peaks for Ag $3d_{5/2}$ and Ag $3d_{3/2}$ at binding energies of 368.1 and 374.1 eV, respectively (Fig. 3f). This is characteristic of Ag^{+} according to the literature.[56]

Optical properties analysis

Fig. 4a shows the UV-Vis diffuse reflectance spectra of $ZnFe_2O_4$, AgI and ZA-10%, 30%, 50%, and 70%. All samples showed strong absorption in the visible region, especially $ZnFe_2O_4$, and the absorption edges of $ZnFe_2O_4$ and AgI were about 583 and 452 nm, respectively. For the composites, the light absorption initial increased gradually and then decreased with respect to

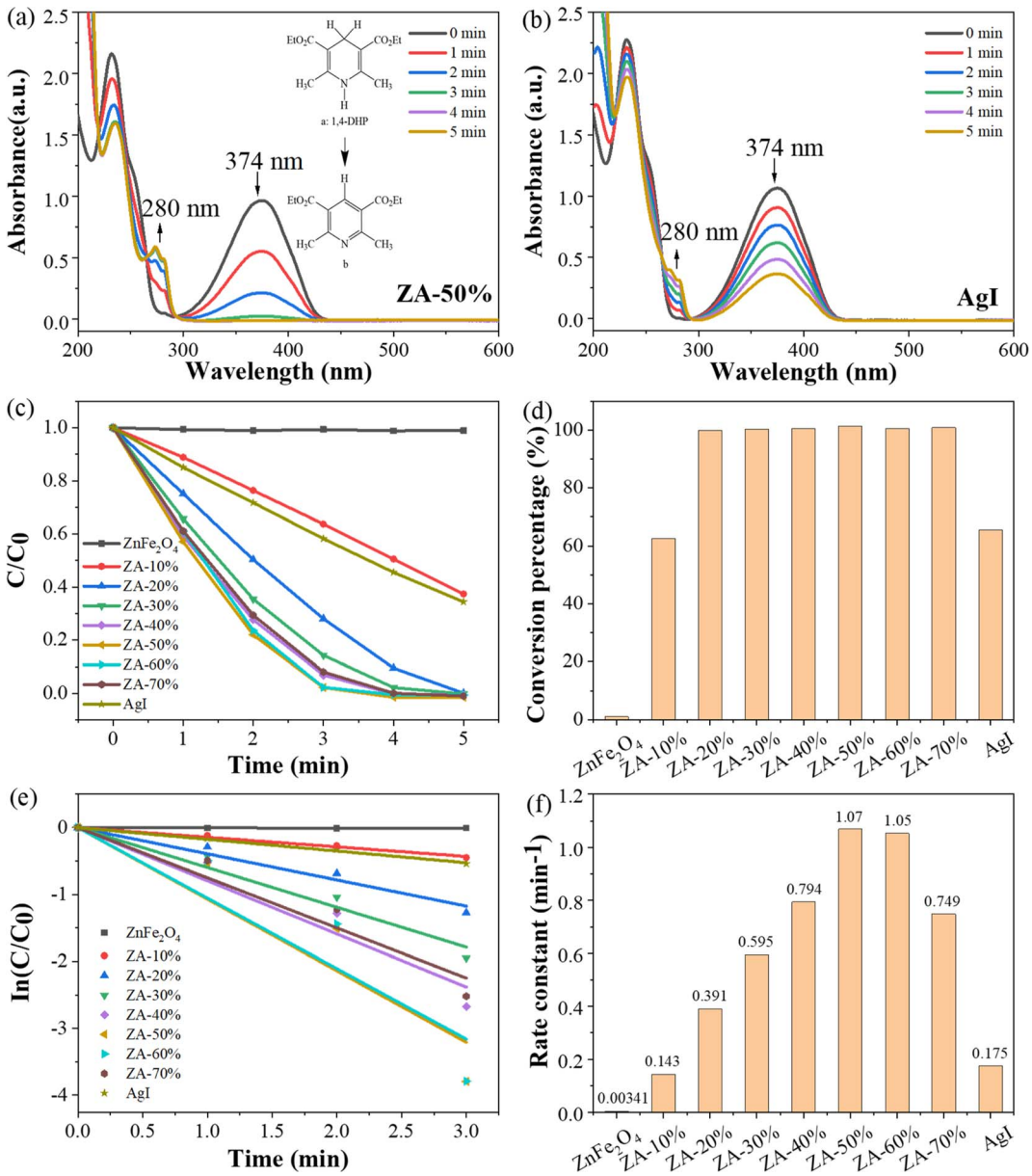

Fig. 6 UV-Vis spectral changes of the 1,4-DHP solution in the presence of ZA-50% (a), AgI (b); $ZnFe_2O_4$, AgI and ZA-*x*% photocatalytic oxidation of 1,4-DHP: kinetic diagram (c), dehydrogenation efficiency diagram (d), linear kinetic fitting graph (e), Pseudo-first-order rate constants (f) under visible light irradiation ($\lambda \geq 400$ nm).

the mass ratio of AgI. The band-gap energy (E_g) of $ZnFe_2O_4$ and AgI were calculated from the DRS data and Kubelka–Munk formula:[14]

$$(\alpha h\nu) = A(h\nu - E_g)^{n/2}$$

where α is the absorption coefficient, h is the Planck constant, ν is the incident light frequency, A is a constant, E_g is the band gap energy and n is an integer. The n depends on where the semiconductor is direct ($n = 1$) or indirect ($n = 4$). Both $ZnFe_2O_4$ (ref. 21 and 37) and AgI[14,61] are direct semiconductors ($n = 1$), and the E_g values $ZnFe_2O_4$ (1.89 eV) and AgI (2.68 eV) were obtained by plotting $(\alpha h\nu)^2$ *versus* $h\nu$ and extrapolating the straight line to the horizontal axis (Fig. 4b).

Electrochemistry analysis

Mott–Schottky plots were measured within the voltage from −1.0 to 1.0 V to derivate the type and energy band position of the semiconductors. The positive slope of the curves (Fig. 5) indicated that both $ZnFe_2O_4$ and AgI are n-type semiconductors. The flat-band potentials of $ZnFe_2O_4$ and AgI were −0.53 V (Fig. 5a) and −0.47 V (Fig. 5b) (*vs.* Ag/AgCl), respectively. According to the equation of E_{NHE} (V) = $E_{Ag/AgCl}$ (V) + 0.197 V, the flat-band potentials of $ZnFe_2O_4$ and AgI were −0.33 V and −0.27 V (*vs.* NHE). In generally, the flat-band potential of an n-type semiconductor is 0.1 V lower than the conduction band (CB) potential (E_{CB}).[59,62] Therefore, the CB potentials of $ZnFe_2O_4$ and AgI were about −0.43 and −0.37 V (*vs.* NHE), respectively.

The valence band (VB) potential (E_{VB}) were calculated using the following formula:[45]

$$E_{VB} = E_{CB} + E_g$$

The VB potentials of $ZnFe_2O_4$ and AgI were calculated to be 1.46 and 2.31 V (*vs.* NHE), respectively.

From Fig. 5c, it could be seen that the ZA-50% displayed the highest photocurrent density under light irradiation, indicating that the separation efficiency of e^- and h^+ were the highest. Similarly, the differences in charge carriers can be seen by comparing the arc radius from the electrochemical impedance spectra (EIS) Nyquist and a smaller radius indicates superior electronic conductivity and faster charge transfer.[63] The arc radius of ZA-50% was the smallest (Fig. 5d), indicating that its photogenerated carriers had the best transmission speed after photoexcitation,[64] inhibiting the recombination of photogenerated carriers.

Evaluation of photocatalytic performance

The photocatalytic activity of the $ZnFe_2O_4$/AgI composite was evaluated by the photocatalytic dehydrogenation of 1,4-DHP under visible light irradiation ($\lambda \geq 400$ nm). As shown in Fig. 6a, the intensity of the characteristic peak of 1,4-DHP (374 nm)

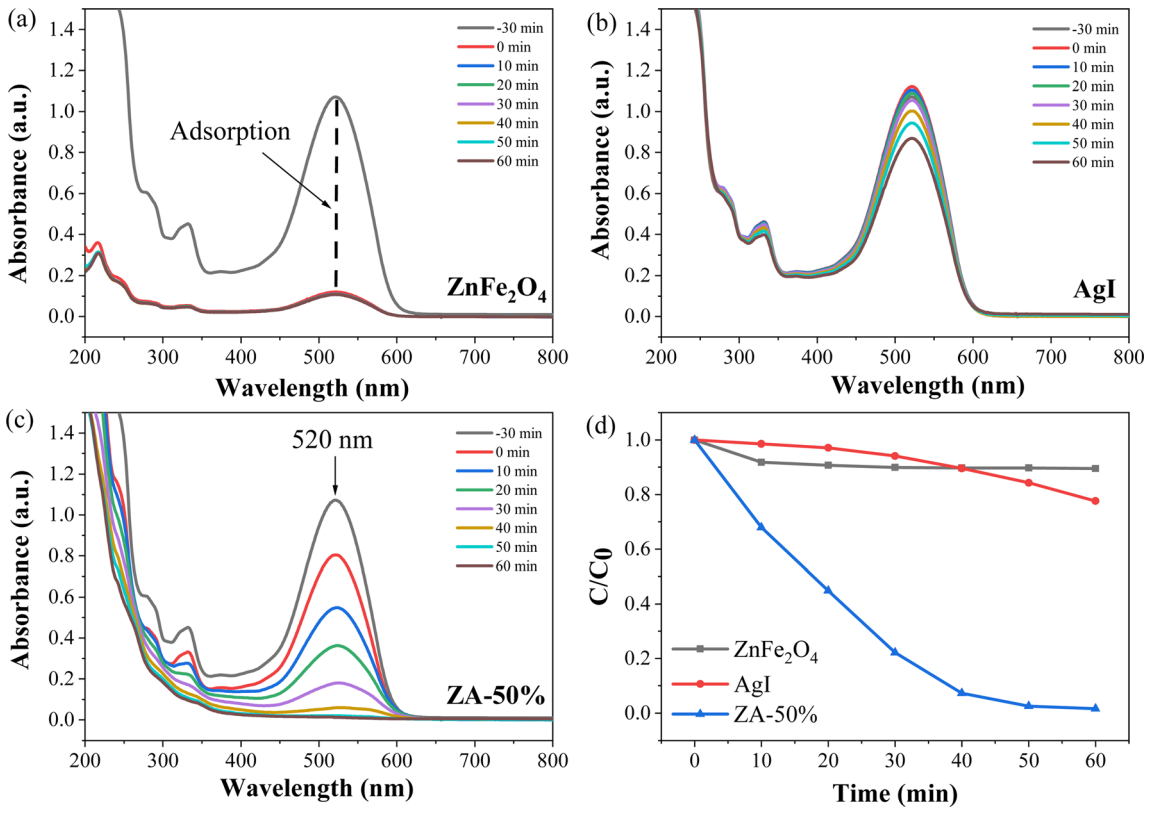

Fig. 7 UV-vis spectral changes of the AM solution under visible light irradiation ($\lambda \geq 400$ nm) in the presence of $ZnFe_2O_4$ (a), AgI (b), ZA-50% (c), the kinetic diagram of $ZnFe_2O_4$, AgI and ZA-50% to degrade AM (30 mg L^{-1}) (d).

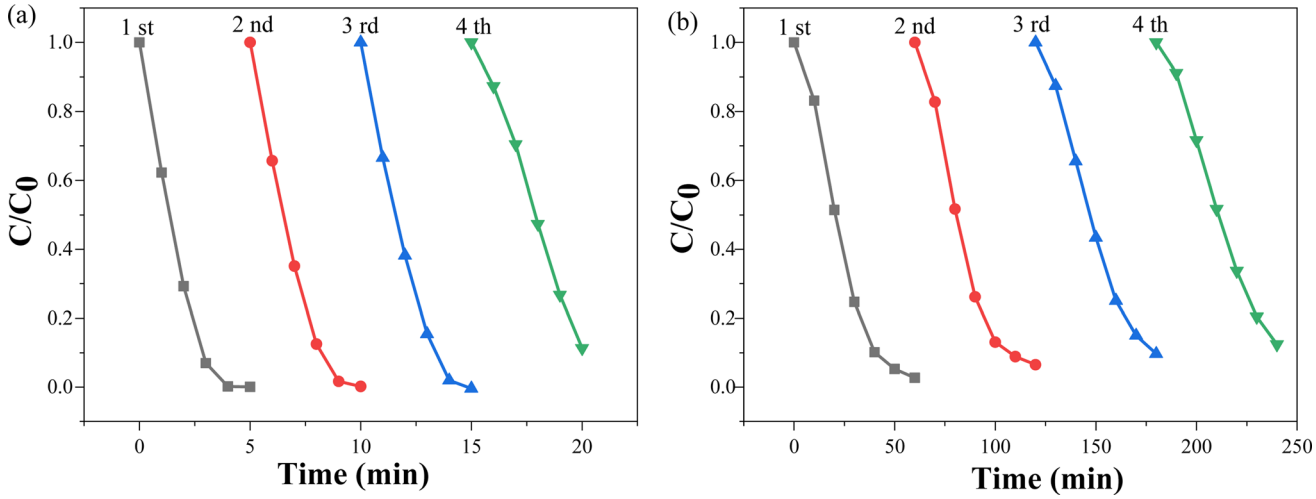

Fig. 8 Cyclic kinetics curve of photooxidation of 1,4-DHP (a) and photodegradation of AM (b) by ZA-50%.

decreased rapidly, accompanied by the emergence of a new peak at 280 nm[46] in the presence of ZA-50% composite. This indicates the rapid removal of two hydrogen atoms from the six-membered ring of 1,4-DHP, effectively converting it to its pyridine derivatives[45] (Fig. 6a, inset). The absorption peak of 1,4-DHP at 374 nm also decreased in the presence of AgI (Fig. 6b), but at a much slower rate compared with ZA-50%. However, there was almost no change observed in the UV-Vis spectra of 1,4-DHP in the presence of $ZnFe_2O_4$ (data not shown).

To investigate the impact of AgI proportion on the photocatalytic activity of the composites, photocatalytic dehydrogenation of 1,4-DHP was conducted at various AgI ratios (Fig. 6c). It was observed that the conversion of 1,4-DHP to its pyridine derivatives was completely executed with 5 min when the AgI content ranged from 20% to 70% (Fig. 6c and d). The plots of $\ln(C/C_0)$ *versus* reaction time were analyzed in order to determine the pseudo-first-order rate constants of the dehydrogenation reaction (Fig. 6e). The rate constants calculated from Fig. 6e were compared in Fig. 6f. All the composites exhibited an increased rate constants compared to AgI and $ZnFe_2O_4$. The ZA-50% sample displayed the highest rate constant (1.07 min^{-1}), which was approximately 313 times higher than that of $ZnFe_2O_4$ (0.00341 min^{-1}) and 6 times higher than that of AgI (0.175 min^{-1}), respectively (Fig. 6f).

To further investigate the photocatalytic capability of the composite catalyst, an organic dye, AM, was selected for photodegradation. It was observed $ZnFe_2O_4$ exhibited a strong adsorption capacity and but almost no catalytic activity (Fig. 7a). On the other hand, AgI showed minimal adsorption capacity and weaker catalytic activity (Fig. 7b) compared to ZA-50% (Fig. 7c). The adsorption capacity of ZA-50% fell between that of $ZnFe_2O_4$ and AgI, while demonstrating the best photocatalytic ability by degrading 98.4% of AM in just 60 min (Fig. 7c and d). Furthermore, degradation experiments for MO and indole were carried out as detailed in the ESI (Fig. S1 and S2).†

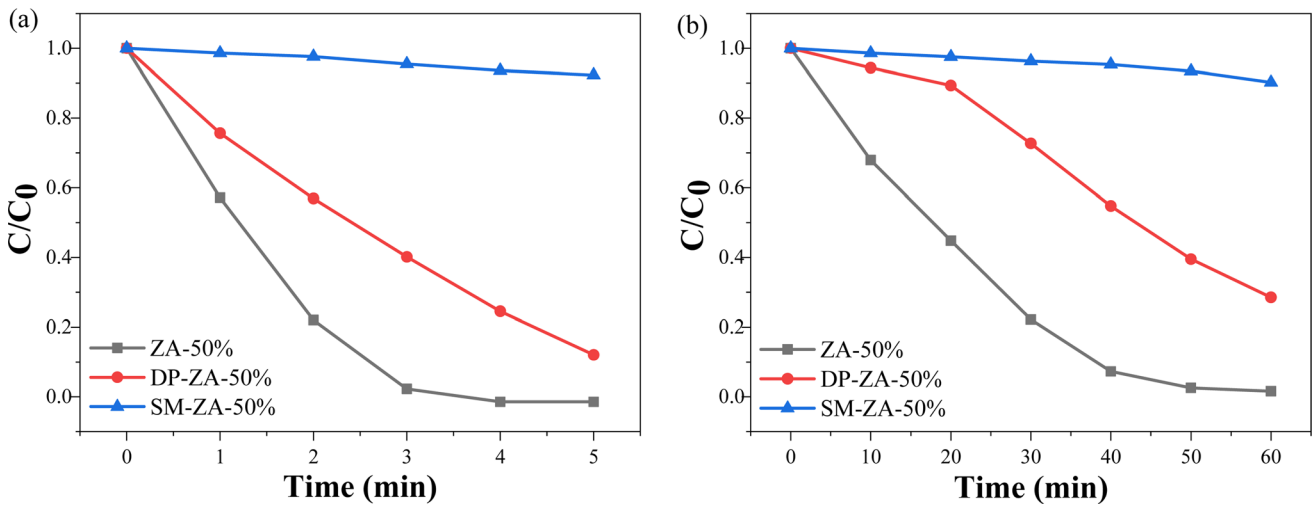

Fig. 9 Kinetics of photo-oxidative dehydrogenation of 1,4-DHP (a), photocatalytic degradation of AM (b) by ZA-50%, DP-ZA-50%, SM-ZA-50% under visible light.

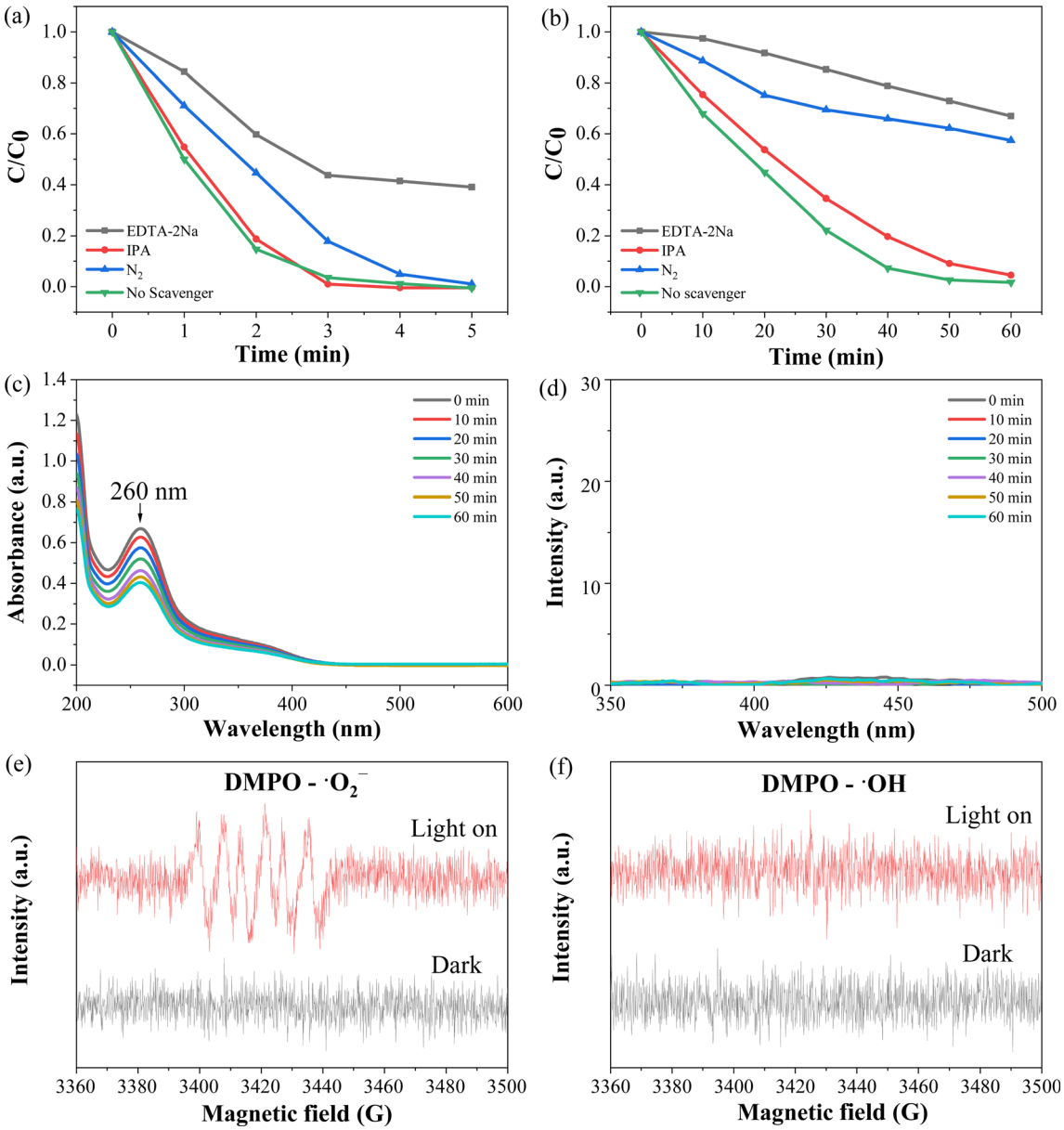

Fig. 10 The effect of certain selected scavengers on the photooxidation of 1,4-DHP and photodegradation of AM by ZA-50% under visible light ($\lambda \geq 400$ nm): kinetic diagrams of 1,4-DHP oxidation (a) and AM degradation (b); UV-Vis absorption spectrum evolution of nitroblue tetrazolium solution (c); fluorescence spectra of TA solution (d); EPR signals of DMPO-$^{\bullet}O_2^-$ adducts (e), and DMPO-$^{\bullet}$OH adducts (f) in the presence of ZA-50%.

In a word, it was clearly that the $ZnFe_2O_4$/AgI composite photocatalyst displayed better catalytic activity than that of $ZnFe_2O_4$ and AgI.

In order to assess the stability of the composite, the catalysts on the filter membrane and in the reactor were recovered and reused for four cycles of catalytic process. Despite a slight reduction in photocatalytic efficiency, the 1,4-DHP dehydrogenation rate remained high at 88.7% (Fig. 8a) and the AM degradation rate was 87.6% (Fig. 8b) after four cycles.

To demonstrate the superiority of ball milling method, ZA-50% was compared with DP-ZA-50% and SM-ZA-50%. In both dehydrogenation of 1,4-DHP (Fig. 9a) and degradation of AM (Fig. 9b), ZA-50% showed the highest photocatalytic activity, surpassing that of DP-ZA-50%, while SM-ZA-50% exhibited the weakest photocatalytic ability.

Photocatalytic mechanism

It is widely accepted that the main active species in photocatalysis are photogenerated holes (h^+), hydroxyl radicals ($^{\bullet}OH$) and superoxide radicals ($^{\bullet}O_2^-$), and these primary active species can be detected through trapping experiments using specific scavengers.[14,23] As shown in Fig. 10a and b, the addition of EDTA-2Na as a hole scavenger[65] significantly inhibited the photocatalytic reaction, indicating that h^+ play a crucial role in

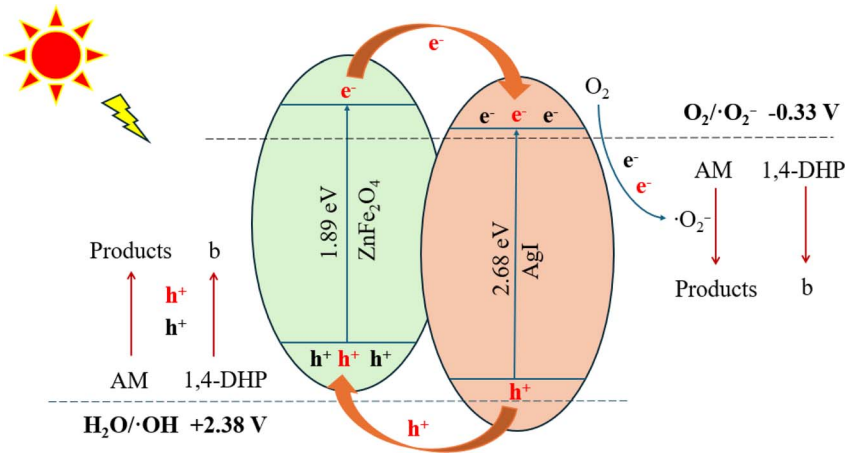

Fig. 11 Hypothetical mechanism diagram of photooxidation of 1,4-DHP and photodegradation of AM by $ZnFe_2O_4$/AgI composite under visible light ($\lambda \geq 400$ nm).

photocatalysis. Additionally, the removal of dissolved O_2 through N_2 bubbling resulted in a decrease in photocatalytic efficiency, suggesting that $^{\bullet}O_2^-$ is also involved in the photocatalytic process since it is generated by the reduction of O_2 with photogenerated electrons ($O_2 + e^- \rightarrow {}^{\bullet}O_2^-$).[44,66,67] However, the introduction of isopropyl alcohol (IPA) as a $^{\bullet}OH$ scavenger exhibited minimal inhibitory effects, implying that $^{\bullet}OH$ may not participate in the photocatalytic process.[44]

To further validate the generation of active species during the photocatalysis, NBT was employed to illustrate the generation of $^{\bullet}O_2^-$ radicals.[43] The decreased peak intensity at 260 nm indicated the production of $^{\bullet}O_2^-$ (Fig. 10c). Moreover, a fluorescence method[68,69] was utilized to determine the generation of $^{\bullet}OH$ radicals. Nanosized TiO_2 (Degussa P25) was also employed as a reference, as detailed in the ESI (Fig. S3).† As shown in Fig. 10d, no distinct peak at 425 nm was observed, indicating that $^{\bullet}OH$ radicals were not generated during the photocatalytic process in the presence of ZA-50% composite. Additionally, electron paramagnetic resonance (EPR) measurements revealed the production of $^{\bullet}O_2^-$ under light irradiation in the presence of ZA-50% composite sample (Fig. 10e). However, it was observed that $^{\bullet}OH$ was not generated (Fig. 10f).[32,70]

Based on the above observations, a reasonable mechanism is proposed in Fig. 11. Under visible light, $ZnFe_2O_4$ and AgI are excited, generating e^- in the CB and h^+ in the VB. Electrons in the CB of $ZnFe_2O_4$ are transferred to the CB of AgI, which has a more negative potential than the standard redox potential of $O_2/^{\bullet}O_2^-$ (−0.33 V *vs.* NHE).[43] This leads to the reduction of O_2 to $^{\bullet}O_2^-$, resulting in the degradation of AM and dehydrogenation of 1,4-DHP to pyridine derivatives. Similarly, the h^+ in the VB of AgI are transferred to the VB of $ZnFe_2O_4$ for degradation of AM and dehydrogenation of 1,4-DHP. Both of $ZnFe_2O_4$ and AgI have a more negative VB potential than $H_2O/^{\bullet}OH$ (+2.38 V *vs.* NHE),[45] so no $^{\bullet}OH$ radicals can be generated, consistent with previous trapping experiments and the EPR results. The enhanced photocatalytic activity of $ZnFe_2O_4$/AgI composite is attributed to the efficient charge separation enabled by the heterojunction formation.

Conclusion

$ZnFe_2O_4$/AgI composites were prepared using a ball-milling method, exhibiting enhanced photocatalytic activity under visible light compared to $ZnFe_2O_4$ and AgI. Among these composites, the $ZnFe_2O_4$/AgI-50% sample exhibited the most effective catalytic activity, completely oxidizing 1,4-DHP in just 5 minutes. The degradation efficiency of AM reached 98.4% within 1 hour, MO reached 89.3% within 3 hours, and indole reached 70.9% within 1 hour. The pseudo-first-order rate constants of $ZnFe_2O_4$/AgI-50% were found to be significantly higher than that of AgI for the photooxidation of 1,4-DHP (6 times), AM (20 times), MO (64 times), and indole (38 times). Mechanism experiments confirmed that h^+ and $^{\bullet}O_2^-$ played a primary role in the catalytic process. The enhanced photocatalytic activity of $ZnFe_2O_4$/AgI composite is attributed to efficient charge separation and transfer enabled by heterojunction formation. This composite shows promise for use in other fields due to its efficient photocatalytic ability.

Data availability

All relevant data are within the manuscript and its additional files.

Conflicts of interest

There are no conflicts of interest to declare.

Acknowledgements

This work was supported by the Opening Project of Chemical Synthesis and Pollution Control Key Laboratory of Sichuan Province (CSPC2016-3-2) and the Opening Project of Key Laboratory of Green Chemistry of Sichuan Institutes of Higher Education (LZJ2002).

References

1 R. Navarro, M. Sanchez-Sanchez, M. Alvarez-Galvan, F. Del Valle and J. Fierro, *Energy Environ. Sci.*, 2009, **2**, 35–54.
2 J. Liu, S. Zhang, W. Wang and H. Zhang, *J. Energy Chem.*, 2023, **86**, 84–117.
3 N. Askari, M. Jamalzadeh, A. Askari, N. Liu, B. Samali, M. Sillanpaa, L. Sheppard, H. Li and R. Dewil, *J. Environ. Sci.*, 2024, **148**, 283–297.
4 H. He, S. Xue, Z. Wu, C. Yu, K. Yang, G. Peng, W. Zhou and D. Li, *Chin. J. Catal.*, 2016, **37**, 1841–1850.
5 N. Chumha, W. Pudkon, A. Chachvalvutikul, T. Luangwanta, C. Randorn, B. Inceesungvorn, A. Ngamjarurojana and S. Kaowphong, *Mater. Res. Express*, 2020, **7**, 015074.
6 H. He, J. Li, C. Yu and Z. Luo, *Sustainable Mater. Technol.*, 2019, **22**, e00127.
7 T. Yang, P. Deng, L. Wang, J. Hu, Q. Liu and H. Tang, *Chin. J. Struct. Chem.*, 2022, **41**, 2206023–2206030.
8 X. Tao, Y. Wang, J. Qu, Y. Zhao, R. Li and C. Li, *J. Mater. Chem. A*, 2021, **9**, 19631–19636.
9 W. Fu, J. Fan and Q. Xiang, *Chin. J. Struct. Chem.*, 2022, **41**, 2206039–2206047.
10 S. Kumari, K. Sharma, S. Korpal, J. Dalal, A. Kumar, S. Kumar and S. Duhan, *CrystEngComm*, 2024, **258**, 120694.
11 Y. Zeng, D. Lu, K. Kondamareddy, H. Wang, Q. Wu, H. Fan, Q. Wang, B. Zhang, L. Xie and Y. Zhang, *J. Alloys Compd.*, 2022, **908**, 164642.
12 J.-W. Hong, *Catalysts*, 2021, **11**, 848.
13 Y. Zhou, S. Fang, M. Zhou, G. Wang, S. Xue, Z. Li, S. Xu and C. Yao, *J. Alloys Compd.*, 2017, **696**, 353–361.
14 H. Luo, S. Dong, H. Li, S. Chen, J. Huang and K. Xu, *Opt. Mater.*, 2023, **140**, 113842.
15 J. He, Y. Cheng, T. Wang, D. Feng, L. Zheng, D. Shao, W. Wang, W. Wang, F. Lu, H. Dong, R. Zheng and H. Liu, *Appl. Surf. Sci.*, 2018, **440**, 99–106.
16 P. Minu and A. Santhi, *IOP Conf. Ser.: Mater. Sci. Eng.*, 2022, **1233**, 012001.
17 I. Muhammad, R. Faria, S. Muhammad, A. Hafiz and W. Sadia, *Sci. Prog.*, 2019, **102**, 61–72.
18 M. Su, C. He, V. Sharma, M. Asi, D. Xia, X. Li, H. Deng and Y. Xiong, *J. Hazard. Mater.*, 2012, **211–212**, 95–103.
19 M. Tsvetkov, J. Zaharieva and M. Milanova, *Catal. Today*, 2020, **357**, 453–459.
20 M. Zhang, X. Xie, Y. Si, J. Gao, H. Du, S. Pei, X. Zhang and Q. Yan, *J. Mater. Sci.: Mater. Electron.*, 2019, **30**, 8055–8063.
21 W. Zhao, Z. Wei, C. Li and M. Ding, *Mater. Res. Bull.*, 2024, **169**, 112508.
22 Y. Li, Y. Meng, X. Liu, M. Xiao, Q. Hu, R. Li, X. Ke, G. Ren and F. Zhu, *J. Power Sources*, 2019, **442**, 227256.
23 A. Ma, Y. Gao, D. Zhang and X. Hou, *Surf. Innovations*, 2021, **9**, 139–148.
24 J. Yang, X. Huo, Z. Li, H. Li, T. Wang and S. Ma, *Processes.*, 2023, **11**, 1607.
25 E. Skliri, J. Miao, J. Xie, G. Liu, T. Salim, B. Liu, Q. Zhang and G. Armatas, *Appl. Catal., B*, 2018, **227**, 330–339.
26 S. Sonu, D. Sheetal, R. Vishal, H. Pankaj, T. Ahmad, N. Vijay, V. VanLe and Q. Pardeep, *J. Environ. Chem. Eng.*, 2021, **9**, 105812.
27 K. Spilarewicz, K. Urbanek, A. Jakimínska and W. Macyk, *J. CO_2 Util.*, 2023, **75**, 102574.
28 F. Dai, R. Zhao, X. Huai, J. Han, L. Wang and S. Feng, *Composites, Part B*, 2019, **173**, 106891.
29 L. Zhang and H. Zhang, *Nanoscale Res. Lett.*, 2022, **17**, 114.
30 Y. Zhou, H. An, G. Li, J. Wen, C. Yin, J. Wan, H. Wang, J. Zhang and J. Zhang, *ACS Sustainable Chem. Eng.*, 2024, **12**, 12553–12561.
31 I. V. Esarev, B. Karge, H. Zeng, P. Lippmann, P. G. Jones, H. Schrey, M. Brönstrup and I. Ott, *ACS Infect. Dis.*, 2024, **10**, 1753–1766.
32 Y. Quan, M. Liu, H. Wu, X. Tian, L. Dou, C. Ren and Z. Wang, *Appl. Surf. Sci.*, 2024, **664**, 160212.
33 Y. Shi, J. Ma, Y. Chen, Y. Qian, B. Xu, W. Chu and D. An, *Sci. Total Environ.*, 2022, **804**, 150024.
34 Z.-M. Chen and Z. Zhang, *Rare Met.*, 2023, **42**, 1050–1055.
35 X. Xue, Z. Wang, H. Nie, Z. Yuan, J. Wang, C. Xu, K. Wen and C. Yu, *Rare Met.*, 2024, **43**, 4476–4492.
36 M. Ren, J. Chen, P. Wang, J. Hou, J. Qian, C. Wang and Y. Ao, *J. Colloid Interface Sci.*, 2018, **532**, 190–200.
37 Y. Xu, Q. Liu, M. Xie, S. Huang, M. He, L. Huang, H. Xu and H. Li, *J. Colloid Interface Sci.*, 2018, **528**, 70–81.
38 D. Wei, Y. Quan, X. Ou, M. Feng, M. Liu, Z. Cheng and Z. Wang, *Mater. Lett.*, 2024, **375**, 137237.
39 L. Yang, M. Gao, B. Dai, X. Guo, Z. Liu and B. Peng, *Appl. Surf. Sci.*, 2016, **386**, 337–344.
40 C. Thambiliyagodage and R. Wijesekera, *Curr. Res. Green Sustainable Chem.*, 2022, **5**, 100236.
41 X. Luo, L. Xu, L. Yang, J. Zhao, T. Asefa, R. Qiu and Z. Huang, *ACS Appl. Mater. Interfaces*, 2024, **16**, 18671–18685.
42 Y. Hu, B. Li, C. Yu, H. Fang and Z. Li, *Mater. Today*, 2023, **63**, 288–312.
43 Y. Quan, M. Liu, H. Wu, X. Tian, L. Dou, Z. Wang and C. Ren, *Appl. Surf. Sci.*, 2024, **642**, 158601.
44 Z. Tong, L. He, C. Ren, Z. Wang and Z. Jiang, *Mater. Lett.*, 2018, **217**, 296–299.
45 Y. Cheng, L. He, G. Xia, C. Ren and Z. Wang, *New J. Chem.*, 2019, **43**, 14841–14852.
46 J. Zhang, X. An, N. Lin, W. Wu, L. Wang, Z. Li, R. Wang, Y. Wang, J. Liu and M. Wu, *Carbon*, 2016, **100**, 450–455.
47 N. Shee and H. Kim, *Molecules*, 2023, **28**, 6481.
48 M. Samah, S. Merabet, M. Bouguerra, M. Bouhelassa, S. Ouhenia and A. Bouzaza, *Kinet. Catal.*, 2011, **52**, 34–39.
49 H. Sübütay and İ. Şavklıyıldız, *Crystals*, 2023, **13**, 1230.
50 H. He, L. Zeng, X. Peng, Z. Liu, D. Wang, B. Yang, Z. Li, L. Lei, S. Wang and Y. Hou, *Chem. Eng. J.*, 2023, **451**, 138628.
51 S. Bonomi, V. Armenise, G. Accorsi, S. Colella, A. Rizzo, F. Fracassi, L. Malavasi and A. Listorti, *Appl. Sci.*, 2020, **10**, 4775.
52 X. Li, D. Tang, F. Tang, Y. Zhu, C. He, M. Liu, C. Lin and Y. Liu, *Mater. Res. Bull.*, 2014, **56**, 125–133.
53 A. Upreti, Y. Li, N. Khadgi, S. Naraginti and C. Zhang, *RSC Adv.*, 2016, **6**, 32761–32769.

54 X. Zhou, B. Wang, H. Sun, C. Wang, P. Sun, X. Li, X. Hu and G. Lu, *Nanoscale*, 2016, **8**, 5446–5453.
55 K. Wang, S. Zhan, H. Sun, D. Zhang and J. Wang, *Chem. Eng. J.*, 2020, **400**, 125908.
56 H. Guo, H. Niu, C. Liang, C. Niu, D. Huang, L. Zhang, N. Tang, Y. Yang, C. Feng and G. Zeng, *J. Catal.*, 2019, **370**, 289–303.
57 Y. Gizem and D. Meral, *Appl. Surf. Sci.*, 2020, **510**, 145374.
58 L. Yao, W. Wang, T. Zhu, Y. Wang, Y. Liang, J. Fu, J. Wang, Y. Cheng and S. Liu, *Appl. Catal., B*, 2020, **268**, 118460.
59 K. Xue, J. Wang, R. He, T. Yang, Y. Yan, Y. Peng, U. Omeoga and W. Wang, *Sci. Total Environ.*, 2020, **732**, 138963.
60 J. He, Y. Wang, C. Shi, M. Wang, Z. Cao, R. Zhang, X. Sun, J. Bo, W. Li and Z. Yang, *Sep. Purif. Technol.*, 2022, **284**, 120263.
61 M. Tang, Y. Ao, C. Wang and P. Wang, *Appl. Catal., B*, 2020, **270**, 118918.
62 S. Sun, W. Wang, D. Li, L. Zhang and D. Jiang, *ACS Catal.*, 2014, **4**, 3498–3503.
63 W. Chen, T. Liu, T. Huang, X. Liu, J. Zhu, G. Duan and X. Yang, *J. Mater. Sci.*, 2015, **50**, 8142–8152.
64 X. Guo, J. Liu, D. Li, H. Cheng, K. Liu, X. Liu and T. Liu, *Environ. Sci. Pollut. Res.*, 2023, **30**, 62312–62324.
65 H. Lei, M. Wu, Y. Liu, F. Mo, J. Chen, S. Ji, Y. Zou and X. Dong, *Chin. Chem. Lett.*, 2021, **32**, 2317–2321.
66 W. Li, F. Wang, Y. Shi and L. Yu, *Chin. Chem. Lett.*, 2023, **34**, 107505.
67 Y. Chen, C. Chen, Y. Liu and L. Yu, *Chin. Chem. Lett.*, 2023, **34**, 108489.
68 H. Lei, H. Zhang, Y. Zou, X. Dong, Y. Jia and F. Wang, *J. Alloys Compd.*, 2019, **809**, 151840.
69 Z. Wang, H. Yu, Y. Xiao, L. Zhang, L. Guo and X. Dong, *Chem. Eng. J.*, 2020, **394**, 125014.
70 O. Al-Madanat, B. Nunes, Y. AlSalka, A. Hakki, M. Curti, A. Patrocinio and D. Bahnemann, *Catalysts*, 2021, **11**, 1514.